PCCP

Thermodynamic stability of Pd–Ru alloy nanoparticles: Combination of density functional theory calculation, supervised learning, and Wang–Landau sampling

Journal:	*Physical Chemistry Chemical Physics*
Manuscript ID	CP-ART-04-2022-001848.R1
Article Type:	Paper
Date Submitted by the Author:	06-Jun-2022
Complete List of Authors:	Nanba, Yusuke; Shinshu University, Research Initiative for Supra-Materials Koyama, Michihisa; Shinshu University, Research Initiative for Supra-Materials

SCHOLARONE™ Manuscripts

ARTICLE

Thermodynamic stability of Pd–Ru alloy nanoparticles: Combination of density functional theory calculations, supervised learning, and Wang–Landau sampling

Yusuke Nanba,*[a] Michihisa Koyama*[a, b]

Solid-solution alloy nanoparticles (NPs) comprising Pd and Ru, which are immiscible in the bulk state, have been synthesised and show excellent catalytic performance. To date, most studies have evaluated the stability of alloy NPs at 0 K only. Because the thermodynamic stability of Pd–Ru alloy NPs may differ from that of the alloy in the bulk state, the stable configuration of the NPs must be evaluated under a finite temperature. Such stability evaluations are critical for developing the durable NPs as catalysts. Therefore, the thermodynamic stability of Pd–Ru alloy NPs was analysed using density functional theory (DFT), supervised learning (SL), and Wang–Landau sampling. We calculated the excess energy of Pd–Ru alloy NPs, which depends on their composition, structure, NP size, adatom type, and defects, and applied SL to all models. The excess energies of the Pd–Ru alloy NPs expressed by structural information, such as the surface-to-volume ratio, correlated with those calculated using DFT. Wang–Landau sampling based on the energy estimated by SL gave the thermodynamic stability of Pd–Ru alloy NPs with a stable configuration under a finite temperature. The solid-solution atomic configuration was subdivided into partially mixed configurations in the surface layer or in the core of the NPs, which is different from the bulk state. The partially mixed configuration was determined by the overall composition and surface properties. The findings from the combined method could contribute to a better understanding of the alloy-NP stability and their application in catalysis.

Introduction

Alloys with solid-solution configurations, in which elements are randomly mixed at the atomic scale, are fabricated for specific combinations in the bulk state. The phase diagrams for various binary elements have been clarified.[1] The affinity of the constituent elements, which determines the segregation or solid-solution phase, has been semi-empirically discussed using the electronegativity difference and electron density discontinuity.[2–4]

Recently, solid-solution alloy nanoparticles (NPs) of binary elements that are immiscible in the bulk state have been synthesised.[5–9] Pd–Ru NPs are an example of solid-solution alloy NPs. In the bulk state, Pd and Ru are miscible in Pd- and Ru-rich compositions at 1100–1800 K, while they are immiscible in a composition of approximately 50 at%.[10–12] Kusada *et al.* successfully synthesised solid-solution $Pd_{0.5}Ru_{0.5}$

alloy NPs by a chemical reduction method.[13] The solid-solution $Pd_{0.4}Ru_{0.6}$ and $Pd_{0.5}Ru_{0.5}$ alloy NPs have excellent catalytic properties for CO oxidation,[13] NO_x reduction,[14] and the oxygen evolution reaction.[15] The stable configuration of the alloy NPs is important for ensuring long-term stable catalytic performance. Evaluating the crucial stability factor is expected to enable the design of binary alloy NPs of two elements that are immiscible in the bulk state.

Stability can be described by enthalpy and entropy. To evaluate the enthalpy, the excess energy of NPs[16–18] has been calculated using density functional theory (DFT). For models comprising approximately 50 atoms, the most stable configuration of Pt-based alloy NPs was investigated at different compositions.[16,17] Ishimoto *et al.* discussed the stability of Pd–Pt alloy NPs with different configurations using NP models comprising 711 atoms.[18] The configurational entropy influences the thermodynamic stability of solid-solution Pd–Pt alloy NPs and their stability is highly dependent on the configuration.

In studies of the stability of alloy NPs, many atomic configurations have been considered to determine a stable configuration. It is unrealistic to conduct DFT-based screening to identify a globally stable structure, composition, and atomic configuration because of the high computational cost. Supervised learning (SL) is a useful method to reveal the

factors dominating the properties of the material. For example, DFT studies have been combined with SL to analyse the stability and properties of materials.[19–25] The classification of miscibility and immiscibility was performed for bulk binary alloy systems using DFT and SL techniques and compared with Miedema's semi-empirical method.[26] The combined method was expanded to calculate the molecular adsorption energy on NPs because the inhomogeneity of NPs increases the considerable number of adsorption sites.[25,27] The combination of DFT and SL studies is useful for analysing systems with many configurations, such as alloy NPs. Furthermore, Monte Carlo (MC) simulations combined with DFT and SL enabled the attainment of a stable configuration for alloy NPs at a finite temperature.[28]

To evaluate the thermodynamic stability of Pd–Ru alloy NPs, the influence of the surface formation on the stability needs to be clarified and the entropy effect due to many configurations should be considered. Here, unlike previous studies, the thermodynamic stability of Pd–Ru alloy NPs was analysed by combining DFT calculations, SL, and MC simulations. The dependence of the excess energy on the structure, composition, and size of Pd–Ru alloys was investigated using DFT. Furthermore, SL was conducted to calculate the excess energies to reveal the stability of the Pd–Ru alloy NPs. The obtained descriptors were used in the MC simulation of Pd–Ru alloy NPs. The NP size, structure, and composition of thermodynamic stability of the Pd–Ru alloy NPs were analysed. The new insights related to the stability of Pd–Ru alloy NPs is expected to contribute to the design of highly stable catalyst materials.

Methods

Computational Details

All calculations were conducted using the Vienna ab initio simulation package code based on DFT.[29,30] The Perdew–Burke–Ernzerhof exchange-correlation functionals[31] with a generalized gradient approximation were used. A projector-augmented wave was used for the interaction between valence and core electrons.[32,33] The cut-off energy of the plane-wave basis set was 400 eV. The k-point grid was $1 \times 1 \times 1$ in the NP models, whereas the Monkhorst–Pack k-point grids in the face-centred cubic (fcc) and hexagonal close-packed (hcp) structures were $9 \times 9 \times 9$ and $6 \times 12 \times 8$, respectively, in the bulk models. The convergences of the self-consistent field and geometry optimisation were 1.0×10^{-5} and 1.0×10^{-4} eV, respectively.

Models

In Pd- and Ru-rich compositions, the Pd–Ru alloy shows solid-solution fcc and hcp structures.[10–12] The bulk models in the fcc and hcp structures comprised 32 atoms, as shown in Figures 1 (a) and (b). Pd–Ru alloy NPs have fcc and hcp structures.[13,34] Truncated octahedrons and truncated hexagonal bipyramids comprising 201 and 238 atoms, respectively, were applied as fcc and hcp NP models (Figures 1 (c) and (d)), respectively. In

the NP models, the vacuum space in the unit cell was set to above 12 Å to prevent interactions with neighbouring NPs. In solid-solution alloys, the two elements are randomly mixed. The Warren–Cowley parameter[35] (α) was used to evaluate the homogeneity of the solid-solution state in the alloy models. This parameter is defined as:

$$\alpha = 1 - P_{AB}/c_B, \tag{1}$$

where P_{AB} and c_B represent the probability of finding the B atom surrounding the A atom, and the overall composition (relative stoichiometry) of the B atom, respectively. When α is close to zero, the two elements in the alloy models are randomly mixed. To evaluate the stability of the Pd–Ru alloys in the NP and bulk models, we estimated the excess energy as

$$\varepsilon_{excess} = (\varepsilon_{Pd-Ru} - c_{Pd}\varepsilon_{Pd}^N - c_{Ru}\varepsilon_{Ru}^N)/N, \tag{2}$$

where N is the number of atoms in the NP and bulk models; and ε_{Pd} and ε_{Ru} represent the total energies of the fcc Pd_N and hcp Ru_N, respectively. High-symmetry fcc Pd_{238} and hcp Ru_{201} are not formed. The cohesive energy of a NP was approximately proportional to $N^{-1/3}$, as shown previously.[36–39]
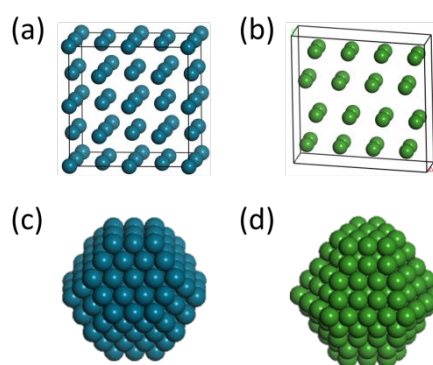

Figure 1 - Models of (a) bulk fcc Pd_{32}, (b) bulk hcp Ru_{32}, (c) fcc Pd_{201}-NP, and (d) hcp Ru_{238}-NP. Truncated octahedron and truncated hexagonal bipyramids were regarded as fcc and hcp NPs, respectively. Blue and green balls represent Pd and Ru atoms, respectively.

The total energies of fcc Pd_{238} and hcp Ru_{201} were estimated from the cohesive energies of Pd and Ru NPs given in the literature.[16,39,40]

Supervised learning

Here, SL was used as a multiple regression analysis method. The hold-out method was used to validate the analysis, and 1/4 and 3/4 of all investigated configurations were randomly selected as the test and training sets, respectively. This validation was repeated five times, and the coefficients of determination (COD) for each case were calculated for the test and training sets.

Wang–Landau sampling

The Wang–Landau sampling method[41,42] was used to calculate the configurational density of states (DOS). The transition probability in the multicanonical MC simulation[43–45] was based on the reciprocal of the configurational DOS, $g(E)$, which is expressed as follows.

$$p(E_A \rightarrow E_B) = \min(1.0, g(E_A)/g(E_B)). \tag{3}$$

2 | *Phys. Chem. Chem. Phys.*, 2012, **00**, 1-3

This journal is © The Royal Society of Chemistry 20xx

When a trial move was accepted, a histogram entry corresponding to the new configuration was implemented. If a move was rejected, a histogram entry corresponding to the old configuration was implemented. The corresponding $g(E)$ was updated by multiplying the existing value by a modification factor f. The $g(E)$ was asymptotically obtained by repeating the calculation until convergence. The flatness criterion of the histogram was set to 0.8 times the average of histogram. When the histogram, $h(E)$, satisfied the flatness criterion, the modification factor was reduced from f to $f^{1/2}$, and the histogram entries were reset to zero. The initial modification factor f_0 was assumed to be Napier's constant e. When f was smaller than $\exp(10^{-8})$, the Wang–Landau sampling was considered completed. The two-dimensional DOS, $g(E, \sigma)$, was used to estimate the structural parameter, σ. It is difficult for the NP model to satisfy the flatness criteria of $h(E, \sigma)$.[46,47] Therefore, a less stringent criterion was used; when the number of entries that were larger than 2000 remained unchanged for $N \times 10^6$ trials, the histogram was regarded as flat.

Results and discussion

Excess energy in Pd–Ru alloys

Figure 2 shows the compositional dependence of the excess energy of the solid-solution Pd_xRu_{N-x} alloy in the bulk and NP states. The specific values of the excess energy and information on the bulk and NP models are presented in Tables S1–6. In the bulk state, the excess energies of fcc and hcp Pd_xRu_{N-x} alloys near c_{Pd} (x/N) = 0.5 exceeded 0.10 eV/atom (Figure 2(a)). The excess energies in the Pd- and Ru-rich compositions were lower than those at c_{Pd} = 0.5. The excess energy of the fcc Pd–Ru alloy was lower than that of the hcp Pd–Ru alloy for the Pd-rich composition, whereas that of the hcp Pd–Ru alloy was lower than that of the fcc Pd–Ru alloy for the Ru-rich composition. In particular, the difference in the Ru-rich composition between the hcp and fcc structures was over 0.10 eV/atom. The compositional dependence of the excess energy had a trend similar to that shown in the phase diagram. As shown in Figure 2(b), the excess energy near c_{Pd} = 0.5 was the highest in Pd_xRu_{N-x} alloy NPs and decreased with an increase or decrease in c_{Pd}, which was the same trend as for the bulk model. However, the standard deviation of the excess energies in the NP models was large compared to that in the bulk model. For the same structure and composition, the excess energies of the NP models were lower than those of the bulk models. For the Ru-rich composition, the fcc Pd–Ru alloy NPs were more stable than the hcp ones. Ru NPs with fcc structure were previously synthesised.[48] In the DFT study, the energy lost during the fcc surface formation was less than that during hcp surface formation.[39] The surface formation may affect the stability of Pd–Ru alloy NPs in Ru-rich compositions. For example, the excess energies of fcc $Pd_{101}Ru_{100}$ and hcp $Pd_{119}Ru_{119}$ increased with increasing Ru content (Figure S1). Here, Pd- and Ru-rich surface-segregated configurations (Figure S2) were considered. The specific values of the excess
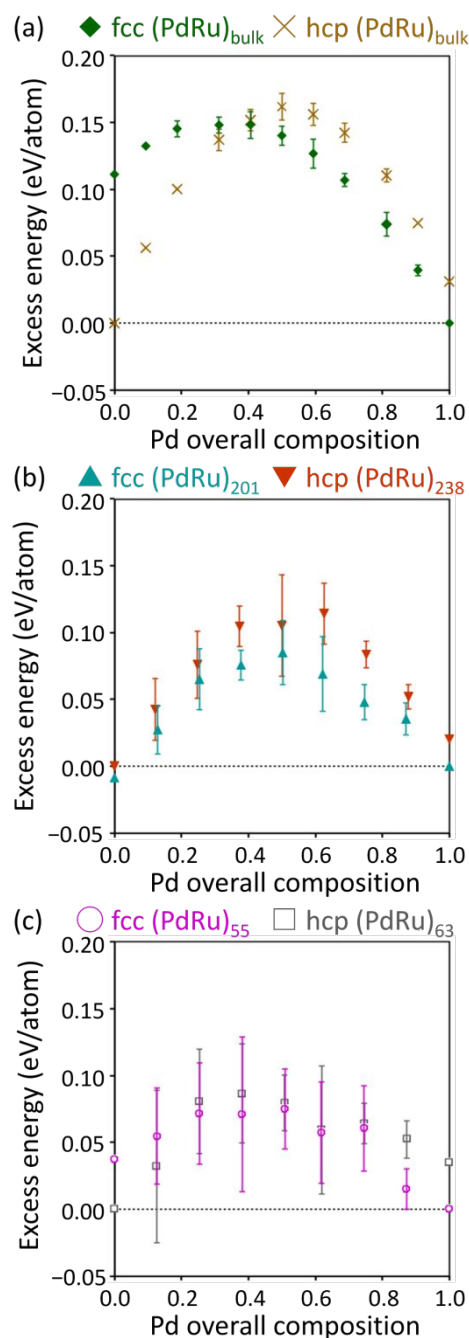

Figure 2 - Compositional dependence of excess energies of (a) solid-solution fcc and hcp Pd–Ru alloys in bulk state, (b) solid-solution fcc $(Pd–Ru)_{201}$ and hcp $(Pd–Ru)_{238}$ alloy NPs, and (c) solid-solution fcc $(Pd–Ru)_{55}$ and hcp $(Pd–Ru)_{63}$ alloy NPs. Symbols and error bars represent average and standard deviation of the excess energies for each composition, respectively.

energy and information on the NP models are summarised in Tables S7 and 8. The excess energies of the Pd-rich surface-segregated configurations were negative. Conversely, the excess energies of the Ru-rich surface-segregated configurations were considerably higher than those of the solid-solution configurations. These characteristic

This journal is © The Royal Society of Chemistry 20xx

Phys. Chem. Chem. Phys., 2013, **00**, 1-3 | **3**

Table 1. Descriptors, corresponding regression coefficients, and standard partial regression coefficient averaged over five cases.

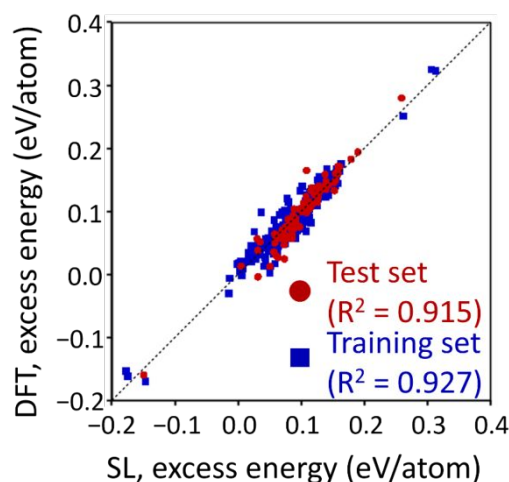| Descriptor		Regression coefficient	Standard partial regression coefficient
(Pd–Pd bond fraction)$_{fcc}$		−0.192	−0.790
(Ru–Ru bond fraction)$_{fcc}$		−0.121	−0.482
(Pd–Pd bond fraction)$_{hcp}$		−0.227	−0.941
(Ru–Ru bond fraction)$_{hcp}$		−0.241	−0.994
ε_{excess}(Ru, bulk)$_{fcc}$ or ε_{excess}(Pd, bulk)$_{hcp}$		−0.738	−0.576
Deviation of Ru	CN = 1–6	1.336	0.386
	CN = 7	1.165	0.416
	CN = 8–11	0.903	0.315
Surface ratio of NP		−0.084	−0.517
Intercept		0.297	0.000

Figure 3 - Comparison of excess energy values determined by supervised learning (SL) and density functional theory (DFT) calculation for Pd–Ru alloy NPs.

configurations affected the excess energy of the Pd–Ru alloy NPs. For example, the excess energy of the subcluster-segregated configuration was lower than that of solid-solution configurations with similar compositions in the surface layer (Tables S7 and 8). We considered well-ordered forms, such as truncated octahedrons and truncated hexagonal bipyramids. High-symmetry NP models have been used in previous theoretical studies.[16–19,36–40] Furthermore, NPs observed by scanning transmission electron microscopy were not highly symmetrical.[5–9,13] There were adatoms and vacancies on the surface of the observed NP.

We investigated the variation in the excess energy using adatoms and defects. A Pd or Ru atom in fcc Pd$_{101}$Ru$_{100}$ and hcp Pd$_{119}$Ru$_{119}$ alloy NPs was added and removed, resulting in eight kinds of Pd–Ru alloy NPs (Figure S3 and Tables S9–16). The addition of a Pd atom to the surface resulted in a lower excess energy than the addition of a Ru atom, whereas the removal of a Pd atom resulted in a higher excess energy than the removal of a Ru atom. These characteristics were similar to the observation that a large Ru composition in the surface layer led to high excess energy. The adatoms and defects decrease the excess energy. As shown in Equation (2), the estimation of excess energy was based on the composition and total energies of monometallic Pd and Ru, and the total energies of Pd and Ru were obtained from the size dependence of the cohesive energy. The differences in the composition and NP size affected the excess energy.

Small-alloy NPs are sensitive to surface formation. We calculated the excess energies of NP models consisting of 55 and 63 atoms in the fcc and hcp structures, respectively. The surface ratios of the NPs were over 0.75. The excess energies of the fcc Pd$_{28}$Ru$_{27}$ and hcp Pd$_{32}$Ru$_{31}$ alloy NPs were lower than those of fcc Pd$_{101}$Ru$_{100}$ and hcp Pd$_{119}$Ru$_{119}$ respectively. The standard deviation of the excess energy was larger than that of larger Pd–Ru alloy NPs. The results of the NP and bulk models suggest that the surface formation affects the stability of the Pd–Ru alloy NPs.

Prediction of Excess Energy of Pd–Ru Alloy NPs

To evaluate stability, SL was applied to the calculated excess energies of the Pd–Ru alloys in the bulk and NP models. The constituent elements of the alloy NPs were fixed. The descriptors were based on the structural information of the bulk and NP models. A total of 410 configurations were considered in this study. For SL, 102 and 308 configurations were used as the test and training sets, respectively. The descriptors were considered based on the configuration dependence of the excess energy. The subcluster-segregated configuration, in which the number of Pd−Ru bonds were limited, had low excess energy compared with the solid-solution configurations. Descriptors related to the bonds are required to predict the excess energy. As shown in Figure S1, the excess energy depended on the Ru composition in the surface layer. Although the slab model had a surface with a constant coordination number (CN), the surface of the truncated octahedron comprised six, seven, eight, and nine CNs expressed as vertices, ridges, (100) facets, and (111) facets, respectively. Adatoms and defects minimally changed the CN. The corresponding atoms were merged with the other CNs. Here, we divided the CN into three groups: CN = 1–6, 7, and 8–11. The composition of the surface layer is affected by the overall composition. In addition, the ratio of the corresponding CN was changed by the NP size, and the type of adatom and defect. With an increase in NP size, the number of atoms in each CN increases. The presence of an adatom and defect increases or decreases the number of atoms in CN 1–6, 7, and 8–11. The Ru deviation in the surface layer, defined as ((Ru composition in each CN) − c_{Ru}) × (ratio of the corresponding CN), was regarded as a descriptor, not the Ru composition of the atoms in each CN. As shown in Table 1, nine descriptors, including the bond fractions of each structure and the surface-to-volume ratio, were used in the SL analysis for determining the excess energy of the Pd–Ru alloy NPs.

4 | *Phys. Chem. Chem. Phys.*, 2012, **00**, 1-3

This journal is © The Royal Society of Chemistry 20xx

Table 2. Coefficients of determination for test and training sets for five cases in Pd–Ru alloy NPs.

	Test set	Training set
(1)	0.910	0.929
(2)	0.889	0.933
(3)	0.952	0.912
(4)	0.913	0.929
(5)	0.884	0.934

Figure 3 shows a representative case comparing the excess energy predicted by SL and that calculated by DFT. The other cases are shown in Figure S4. The excess energies predicted by SL correlated with those calculated using DFT. As shown in Table 2, the COD values for the test and training sets were 0.859–0.913 and 0.911–0.924, respectively. Thus, nine descriptors were used to predict the excess energy of the Pd–Ru alloy NPs. Table 1 presents the coefficients and intercepts of the regression equation. The coefficient of the Pd–Pd bonds in the fcc structure was more negative than that of the Ru–Ru bonds, while that of the Pd–Pd bonds in the hcp structure was less negative than that of the Ru–Ru bonds. In addition, the coefficients in the hcp structure were different from those in the fcc structure. The influence of the bonds depends on the structure. These descriptors cannot be regarded as common descriptors. The coefficient of Ru deviation in the surface layer was positive. The surface energy of Ru was larger than that of Pd (Figure S5 and Table S17). Considering the compositional dependence, the difference between the overall and surface compositions was required to determine the excess energy of the alloy NPs. Table 1 presents the standard partial regression coefficients. The absolute values of the bond fractions were larger than those of other descriptors. Bond fractions are important for predicting the excess energy in the bulk and NP models. The surface formation of the NPs influenced the stability of the alloy NPs. In the NP models, the descriptors related to the surface formation were added to the prediction on the basis of the bond fractions. The excess energy for hcp Pd and fcc Ru in the bulk state and the surface ratio of NPs were included in the nine descriptors. The structure and size dependencies of the excess energy were considered; however, they could not be explained by the common regression intercept. The excess energy of hcp Pd and fcc Ru in the bulk state and the surface ratio of the NP may explain the structure and size dependence of the excess energy.

To validate the size dependence, we applied the obtained regression equation to large Pd–Ru alloy NPs. The models for the solid-solution $Pd_{203}Ru_{202}$, solid-solution $Pd_{356}Ru_{355}$, and subcluster-segregated $Pd_{356}Ru_{355}$ alloy NPs (Figure S6) were prepared, and the NP model information is summarised in Table S18. The model preparation and calculation conditions were the same as those used for the small NPs. The calculated excess energies of solid-solution $Pd_{203}Ru_{202}$, solid-solution $Pd_{356}Ru_{355}$, and subcluster-segregated $Pd_{356}Ru_{355}$ were 0.104, 0.105, and 0.026 eV/atom, respectively. The regression equation was applied to the large Pd–Ru alloy NPs. The excess

fcc $Pd_{128}Ru_{128}$ fcc $Pd_{230}Ru_{26}$
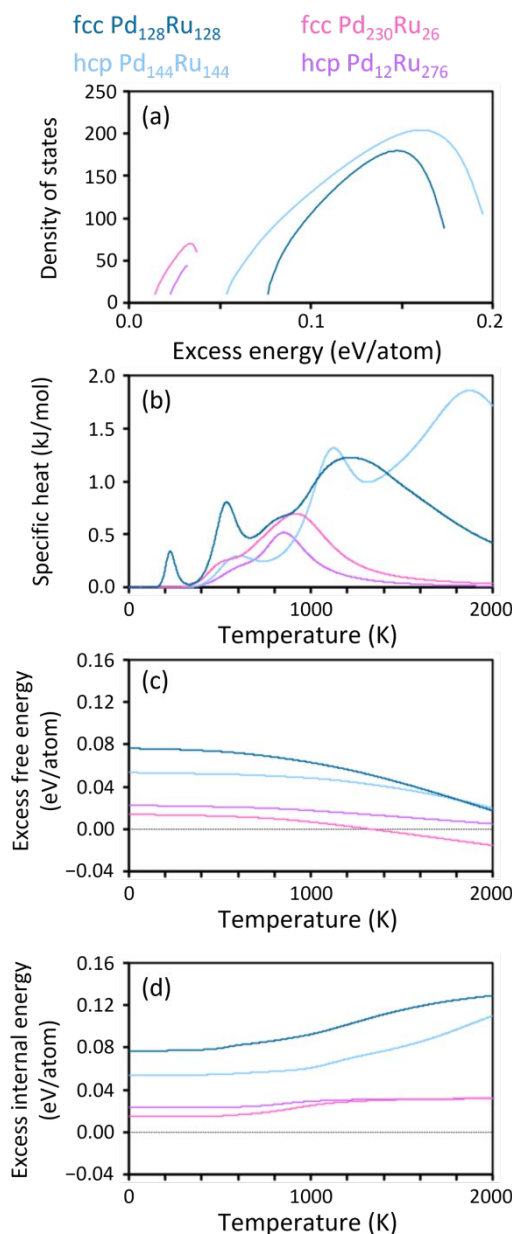hcp $Pd_{144}Ru_{144}$ hcp $Pd_{12}Ru_{276}$

Figure 4 - (a) Configurational DOS, and temperature dependence of (b) configurational specific heat, (c) excess free energy, and (d) excess internal energy in fcc $Pd_{128}Ru_{128}$, fcc $Pd_{230}Ru_{26}$, hcp $Pd_{12}Ru_{276}$, and hcp $Pd_{144}Ru_{144}$.

energies of solid-solution $Pd_{203}Ru_{202}$, solid-solution $Pd_{356}Ru_{355}$, and subcluster-segregated $Pd_{356}Ru_{355}$ estimated using the regression equation were 0.091, 0.090, and 0.034 eV/atom, respectively. The average error in the excess energies using SL and DFT was 0.012 eV/atom for large solid-solution and subcluster-segregated Pd–Ru alloy NPs. The Ru deviation in CN = 8 was not regarded as the separated descriptor although the surface energy of (100) surface is larger than that of (111) surface (Table S17). Only six atoms had a CN of 8 in the Pd_xRu_{201-x} model. The slight difference in atoms with CN = 8 had a significant influence on the excess energy. As the NP size

This journal is © The Royal Society of Chemistry 20xx

Phys. Chem. Chem. Phys., 2013, **00**, 1-3 | **5**

increased, the number of atoms with CN = 7, 8, and 9 increased. Conversely, the number of atoms with CN = 6 was not dependent on the NP size. To enhance the accuracy of the results for larger alloy NPs, subdivision of the descriptor may be needed.

Monte Carlo simulation of Pd–Ru Alloys

fcc $Pd_{128}Ru_{128}$, fcc $Pd_{230}Ru_{26}$, hcp $Pd_{12}Ru_{276}$, and hcp $Pd_{144}Ru_{144}$, where the c_{Pd} were selected according to the phase diagram. The configurational DOS of the considered models was obtained using Wang–Landau sampling (Figure 4(a)). Based on the configurational DOS, the partition function resulted in configurational specific heat (Figure 4(b)), excess free energy (Figure 4(c)), and excess internal energy (Figure 4(d)) at any given temperature.
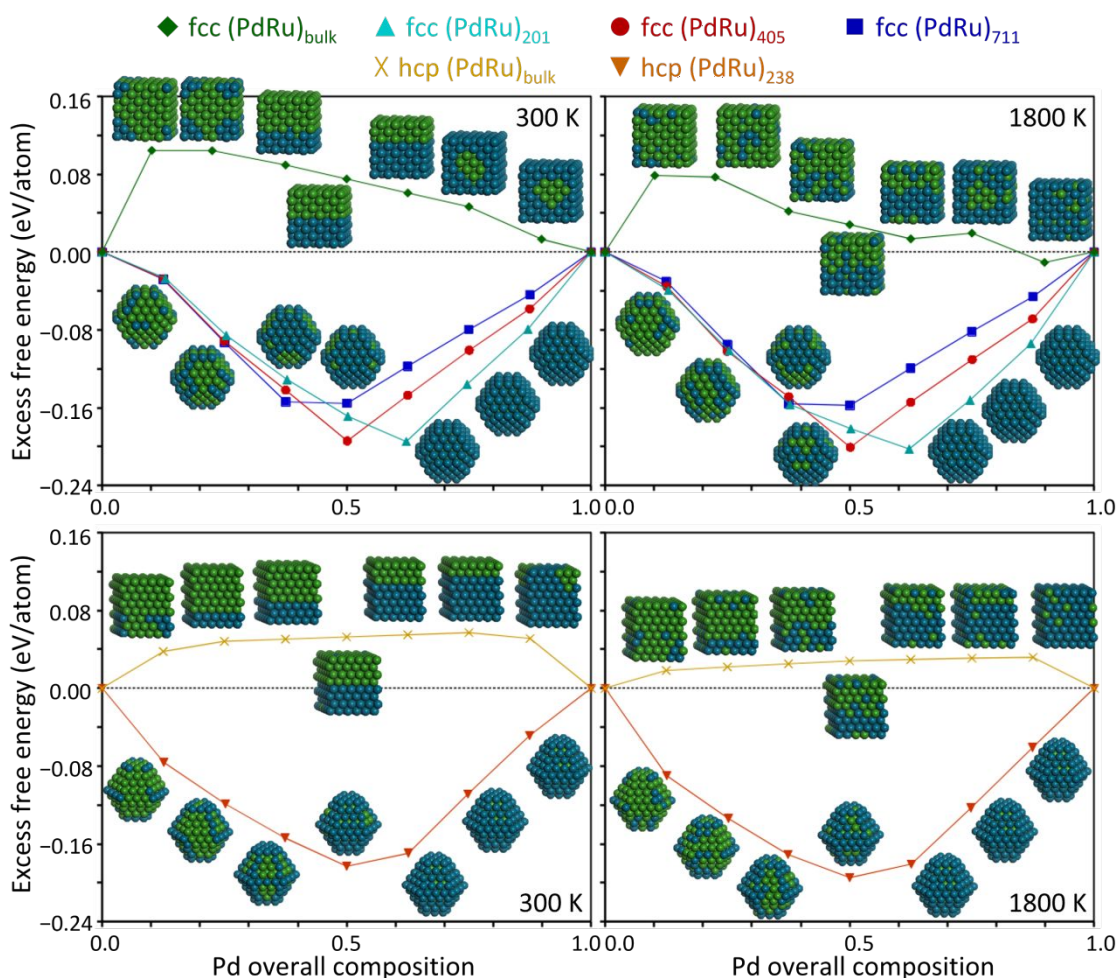

Figure 5 - Pd composition dependence of excess free energies of fcc Pd_xRu_{256-x} and hcp Pd_xRu_{288-x} alloys and fcc Pd_xRu_{N-x} and hcp Pd_xRu_{238-x} alloy NPs at 300 and 1800 K. Blue and green balls represent Pd and Ru atoms, respectively

To understand the thermodynamic stability of the Pd–Ru alloy in the bulk and NP states, we performed Wang–Landau sampling. A regression equation was used to estimate the sampling energy. Notably, the vibrational contribution was not included in the free excess energy. In alloy NPs, the contribution of the configurational entropy difference was considerably larger than that of the vibrational entropy difference.[49] First, we discuss the thermodynamic stability of Pd–Ru alloys in the bulk state. We considered models comprising 256 atoms in the fcc structure (4 × 4 × 4 supercell) and 288 atoms in the hcp structure (6 × 6 × 4 supercell). Figure 4 shows the configurational DOS, configurational specific heat, excess free energy, and excess internal energy in

The peak in the configurational specific heat indicated a change in the stable configuration. Above the corresponding temperature, the slope of the excess free energy increased, whereas the excess internal energy increased. The solid-solution configuration has the advantage of being stabilised by the configurational entropy contribution, but it is disadvantageous in terms of the mixing enthalpy. The energy gain from the configurational entropy effect overcomes the energy loss due to Pd–Ru mixing. There are some peaks in the configurational specific heat curve for fcc $Pd_{128}Ru_{128}$ and hcp $Pd_{144}Ru_{144}$ alloys. However, the excess free energies remained positive, indicating that the Pd–Ru alloy was less stable than the monometallic Pd and Ru below the melting temperature of

6 | *Phys. Chem. Chem. Phys*., 2012, **00**, 1-3

This journal is © The Royal Society of Chemistry 20xx

Pd in the bulk state. The configurational specific heat of the fcc $Pd_{230}Ru_{26}$ alloy showed characteristics similar to those of the fcc $Pd_{128}Ru_{128}$ alloys. However, above 1334 K, the excess free energy of the fcc $Pd_{230}Ru_{26}$ alloy was negative. The expected value of the Warren–Cowley parameter in fcc $Pd_{230}Ru_{26}$ was 0.522 at 300 K and 0.058 at 1800 K, where the temperature of 1800 K below the melting point of Pd in the bulk state was considered. Above 1334 K, the Pd and Ru atoms were homogeneously mixed. In contrast, the excess free energy of the hcp $Pd_{12}Ru_{276}$ alloy was positive. The configurational entropy of the $Pd_{12}Ru_{276}$ alloy may be insufficient for the negative excess free energy. The vibrational entropy due to the volume influences the thermodynamics of the order–disorder transformation in the binary alloy.[50] In this study, the configurational entropy of each energy level was estimated. The vibrational entropy may be non-negligible in the evaluation of stability when the contribution of configurational entropy is small. The solid-solution region of the hcp Pd–Ru alloy was narrower than that of the fcc Pd–Ru alloy. As shown in Table 1, the Pd–Pd and Ru–Ru bonds in the hcp structure had larger absolute regression coefficients than those in the fcc structure. In other words, the excess energy does not decrease when many Pd–Ru bonds are included. The energy loss caused by the solid-solution configuration in the hcp structure may be greater than that in the fcc structure.

Figure 5 shows the overall Pd composition dependence of the excess free energies and stable configurations in fcc Pd_xRu_{256-x} and hcp Pd_xRu_{288-x} alloys, where the configurational DOS, configurational specific heat, excess free energy, excess internal energy, and expected values of the structural parameters are shown in Figures S7–10. Specifically, the excess free energies at 300 and 1800 K were investigated. Warren–Cowley parameters at 300 K were 0.52–0.64 and 0.43–0.73 in the fcc Pd_xRu_{256-x} and hcp Pd_xRu_{288-x} alloys. The large values of Warren–Cowley parameters suggested that the stable configurations of Pd–Ru alloys were segregated types. The transition temperatures of the fcc Pd_xRu_{256-x} and hcp Pd_xRu_{288-x} alloys were below 1800 K. The Pd–Ru bonds increased as shown in Figures S9 and 10. Warren–Cowley parameters at 1800 K were 0.06–0.21 in the fcc Pd_xRu_{256-x} alloys, while those were 0.12–0.45 in the hcp Pd_xRu_{288-x} alloys. The distribution of Pd and Ru atoms becomes more homogeneous. However, the excess free energies of the Pd–Ru alloys were positive, except for fcc $Pd_{230}Ru_{26}$. These modelled properties were close to those observed experimentally and calculated in a previous study.[11,12] Thus, the results obtained by sampling were considered reasonable.

Thermodynamic stability of Pd–Ru Alloy NPs

Wang–Landau sampling was applied to the Pd–Ru alloy NPs. The overall composition dependence of the excess free energies and stable configurations of fcc Pd_xRu_{201-x} and hcp Pd_xRu_{238-x} alloy NPs are shown in Figure 5, where the configurational DOS results are shown in Figures S11 and 12. Stable configurations of the fcc Pd_xRu_{201-x} and hcp Pd_xRu_{238-x} alloy NPs are depicted based on the expected values, such as the composition of each CN and the bond fractions in the
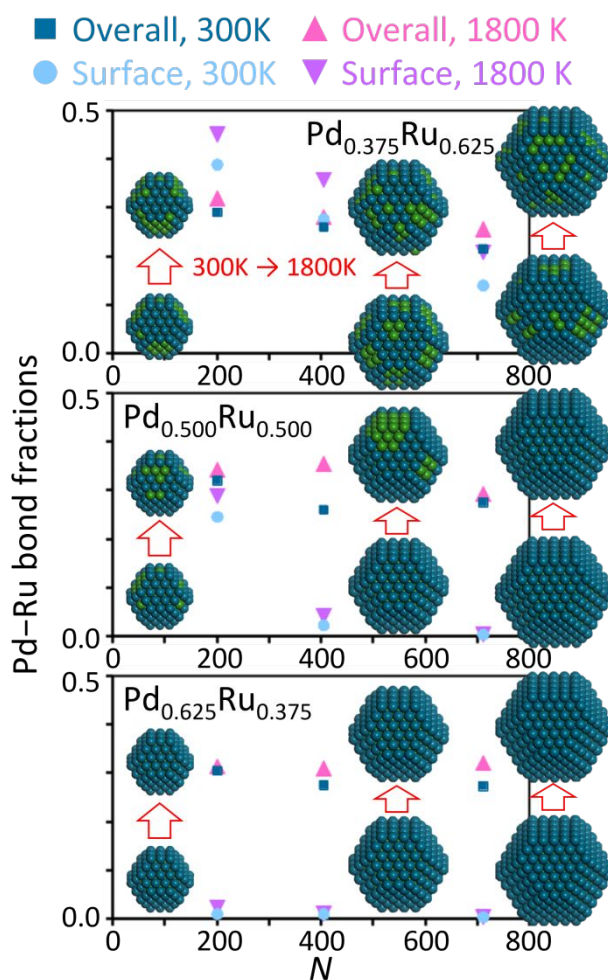

Figure 6 - Size dependence of Pd–Ru bond fractions in fcc $Pd_{0.375}Ru_{0.635}$, fcc $Pd_{0.5}Ru_{0.5}$, and fcc $Pd_{0.625}Ru_{0.375}$ alloy NPs.

entire NP and surface layer (Figures S13 and 14). The stability of the Pd–Ru alloy NPs was drastically different from that of the bulk state. The excess free energy was negative for all compositions. In the stable configuration with $c_{Pd}<0.5$, the Pd atoms occupied low-CN atomic positions, while the Ru atoms occupied the facet (CN = 8 and 9) and core. The stable configuration with $c_{Pd}>0.5$ was a surface-segregated configuration. These characteristics are the same as the stable configuration at 0 K in previous DFT studies of alloy NPs.[16,17] With an increase in temperature, a peak in the specific heat and a change in the excess internal energy were observed (Figures S11 and 12). Thus, the stable configurations of the fcc Pd_xRu_{201-x} and hcp Pd_xRu_{238-x} alloy NPs varied with respect to the bulk state. The temperature dependence of stable Pd–Ru alloy NPs with $c_{Pd}<0.5$ was different from that with $c_{Pd}>0.5$. In $c_{Pd}<0.5$, Ru atoms occupied the ridge and vertex positions (Figures S15 and 16). The Pd atoms in the surface layer were not exchanged with the Ru atoms in the core, even when the temperature increased. In contrast, the Pd atoms in the facet

This journal is © The Royal Society of Chemistry 20xx

Phys. Chem. Chem. Phys., 2013, **00**, 1-3 | **7**

were exchanged with the Ru atoms in the ridge and vertex. Thus, Pd and Ru atoms are mixed in the surface layer. The entropy contribution due to Pd–Ru mixing in the surface layer overcomes the energy loss of Ru atoms at the lower CN atomic position. In contrast, in the c_{Pd}>0.5 case, the surface layer did not change with increasing temperature. However, Warren–Cowley parameters in the fcc Pd_xRu_{201-x} and hcp Pd_xRu_{238-x} alloy NPs changed from 0.21–0.37 (at 300 K) to −0.06–0.21 (at 1800 K). The Pd and Ru atoms in the core were mixed (Figures S15 and 16). The entropy contribution from Pd–Ru mixing in the core overcomes the energy loss of the Pd–Ru bonds. However, in both cases, Pd–Ru mixing did not occur over the entire NP. In the Pd–Ru alloy NPs, the Pd and Ru atoms are partially mixed in the surface layer or in the core of the NP. The Pd–Ru alloy NPs had distinct Pd–Ru mixing behaviour compared to the bulk state.

To investigate the effect of the NP size, fcc Pd_xRu_{405-x} and fcc Pd_xRu_{711-x} were considered. The overall composition dependence of the excess free energies of fcc Pd_xRu_{405-x} and fcc Pd_xRu_{711-x} alloy NPs is shown in Figure 5, and the configurational DOS is shown in Figures S17 and 18. With increasing NP size, the excess free energies of the Pd–Ru alloy NPs became less negative and approached those of the bulk state. The peak of the lowest excess free energy shifted to a lower overall Pd content. The surface ratios of the fcc Pd_xRu_{201-x}, fcc Pd_xRu_{405-x}, and fcc Pd_xRu_{711-x} alloy NPs were 0.607, 0.504, and 0.430, respectively. When the overall Pd composition was equal to the surface ratio of NP, the alloy NPs showed the lowest excess free energy. To discuss the structural characteristic, we investigated the Pd–Ru bond fractions of the Pd–Ru alloy NPs near c_{Pd}=0.5. Figure 6 shows the Pd–Ru bond fractions over the entire NP and the surface layer of the fcc $Pd_{0.375}Ru_{0.625}$, $Pd_{0.5}Ru_{0.5}$, and $Pd_{0.625}Ru_{0.625}$ alloy NPs, along with the stable configurations at 300 K and 1800 K. The expected values of the structural parameters of the fcc Pd_xRu_{405-x} and fcc Pd_xRu_{711-x} alloy NPs are shown in Figures S19 and 20. With an increase in temperature, a peak in the specific heat and change in the excess internal energy were observed (Figures S17 and 18). Thus, in addition to fcc Pd_xRu_{201-x}, the stable configurations of fcc Pd_xRu_{405-x} and fcc Pd_xRu_{711-x} alloy NPs varied, and the Pd–Ru bond fractions in both the entire NP and the surface layer increased. While Warren–Cowley parameters in the fcc Pd_xRu_{405-x} and fcc Pd_xRu_{711-x} alloys were 0.32–0.41 at 300 K, those were 0.16–0.34 at 300 K. The Pd and Ru atoms in both the surface layer of $Pd_{0.375}Ru_{0.625}$ and core of $Pd_{0.625}Ru_{0.375}$ were mixed (Figure S19 and 20). Warren–Cowley parameter in the partially mixed configuration approached zero. The characteristics of large $Pd_{0.375}Ru_{0.625}$ and $Pd_{0.625}Ru_{0.375}$ alloy NPs were the same as those of $Pd_{76}Ru_{125}$ and $Pd_{125}Ru_{76}$ alloy NPs. However, the $Pd_{356}Ru_{355}$ alloy NPs showed different behaviour to the $Pd_{101}Ru_{100}$ alloy NPs. The Pd–Ru bond fraction in the surface layer of the $Pd_{356}Ru_{355}$ alloy NPs was temperature dependent. The Pd and Ru atoms in the core became mixed with increasing temperature (Figure S20), as observed for $Pd_{0.625}Ru_{0.375}$ alloy NPs. The partially mixed configuration was determined by the overall composition and size. Because the structural information is size dependent, the NP size has a significant influence on the stable configuration of the alloy NPs.

Alloys, in which the constituent elements are not mixed at low temperatures, show a solid–solution configuration owing to the entropy effect. In the NP alloy, partial mixing was observed at the surface layer or in the core. The overall composition and NP size play an important role in determining partial mixing. Scanning transmission electron microscopy–energy dispersive X-ray spectroscopy maps revealed that the Pd and Ru atoms are randomly distributed.[13,14] Note that the distribution on a plane is not divided into the contents of the surface layer and core. The partial mixing in the surface layer or core was close to the distribution of the synthesised Pd–Ru alloy NPs. In the Pd–Ru alloy NPs, the contribution of the entropy effect did not overcome the energy loss due to the surface Ru atoms. When the difference between the surface energies of the constituent elements is small, the elements in both the surface layer and core are mixed.[28] The surface formation has a significant influence on the stability of the alloy NP. In DFT calculations, atomic and molecular adsorption affect the surface segregation of alloy NPs.[51,52] In fact, the thermal treatment in a H_2 atmosphere leads to the atomic rearrangement of Pd–Ru alloy NPs.[15] Such adsorption effects are a topic for future research. Various factors, such as NP size and overall composition, and molecular adsorption, determine the stable configuration of alloy NPs. The phase diagram of the alloy NPs is more complicated than that of the bulk state owing to surface effects.

Conclusion

We analysed the thermodynamic stability of Pd–Ru alloy NPs using DFT calculations, SL, and Wang–Landau sampling. SL was performed to determine the excess energies calculated by DFT. The excess energy of the Pd–Ru alloy NPs can be described by structural information. Wang–Landau sampling based on the regression equation of excess energy was used to estimate the configurational DOS, thermodynamic variables, and expected values of the structural parameters. At 300 K, Pd atoms occupy a low-CN atomic position on the NP surface. When the temperature increased, Pd and Ru atoms mixed in the surface layer or in the core. The mixing varies with the overall composition, structure, and NP size. The subdivision of the solid-solution configuration may result in a more complicated phase diagram than that of the bulk state. The surface formation gave a significant influence on the thermodynamic stability of alloy NPs. The composition and size dependence of the thermodynamic stability of alloy NPs were considered in this study, whereas the adsorption effect will be considered in a future work. The adsorption effect is expected to alter the stable configuration of NPs in catalytic activities. If the adsorption energy of the NPs is expressed by structural parameters, Wang–Landau sampling combined with regression equation could reveal the unique thermodynamic stability of catalysis in the operating environment.

8 | *Phys. Chem. Chem. Phys*., 2012, **00**, 1-3

This journal is © The Royal Society of Chemistry 20xx

Author contribution

Conflicts of interest

There are no conflicts to declare.

Acknowledgments

References

1 T. B. Massalski, H. Okamoto, P. R. Subramanian and L. Kacprzak, *Binary Alloy Phase Diagrams; ASM International: Materials Park*, 1996.
2 A. R. Miedema, R. Boom and F. R. de Boer, *J. Less-Common Met.,* 1975, **41**, 283–298.
3 A. R. Miedema, *J. Less-Common Met.,* 1976, **46**, 67–83.
4 A. R. Miedema, P. F. de Châtel and F. R. de Boer, *Physica B+C,* 1980, **100**, 1–28.
5 H. Kobayashi, K. Kusada and H. Kitagawa, *Acc. Chem. Res.,* 2015, **48**, 1551–1559.
6 K. Kusada, M. Yamauchi, H. Kobayashi, H. Kitagawa and Y. Kubota, *J. Am. Chem. Soc.,* 2010, **132**, 15896–15898.
7 B. Huang, K. Kobayashi, T. Yamamoto, S. Matsumura, Y. Nishida, K. Sato, K. Nagaoka, S. Kawaguchi, Y. Kubota and H. Kitagawa, *J. Am. Chem. Soc.,* 2017, **139**, 4643–4646.
8 F. Wang, K. Kusada, D. Wu, T. Yamamoto, T. Toriyama, S. Matsumura, Y. Nanba, M. Koyama and H. Kitagawa, *Angew. Chem. Int. Ed.,* 2018, **57**, 4505–4509.
9 Q. Zhang, K. Kusada, D. Wu, T. Yamamoto, T. Toriyama, S. Matsumura, S. Kawaguchi, Y. Kubota and H. Kitagawa, *Nat. Commun.,* 2018, **9**, 510.
10 A. S. Darling and J. M. Yorke, *Platinum Met. Rev.,* 1960, **4**, 104–110.
11 H. Kleykamp, *J. Nucl. Mater.,* 1989, **167**, 49–63.
12 R. A. Gürler, *J. Alloy Compd.,* 1993, **191**, 31–35.
13 K. Kusada, H. Kobayashi, R. Ikeda, Y. Kubota, M. Takata, S. Toh, T. Yamamoto, S. Matsumura, N. Sumi, K. Sato, K. Nagaoka and H. Kitagawa, *J. Am. Chem. Soc.,* 2014, **136**, 1864–1871.
14 K. Sato, H. Tomonaga, T. Yamamoto, S. Matsumura, N. D. B. Zulkifli, T. Ishimoto, M. Koyama, K. Kusada, H. Kobayashi, H. Kitagawa, K. Nagaoka, *Sci. Rep.,* **6**, 20265.
15 D. Wu, K. Kusada, S. M. Aspera, H. Nakanishi, Y. Chen, O. Seo, C. Song, J. Kim, S. Hiroi, O. Sakata, T. Yamamoto, S. Matsumura, Y. Nanba, M. Koyama, N. Ogiwara, S. Kawaguchi, Y. Kubota, and H. Kitagawa, *ACS Materials Au,* 2021, DOI: 10.1021/acsmaterialsau.1c00048.
16 M. J. Piotrowski and P. Piquini, *J. Phys. Chem. C,* 2012, **116**, 18432–18439.
17 D. Guedes-Sobrinho, R. K. Nomiyama, A. S. Chaves, M. J. Piotrowski and J. L. F. Da Silva, *J. Phys. Chem. C,* 2015, **119**, 15669–15679.
18 T. Ishimoto and M. Koyama, *J. Phys. Chem. Lett.,* 2016, **7**, 736–740.
19 A. Seko, T. Maekawa, K. Tsuda and I. Tanaka, *Phys. Rev. B,* 2014, **89**, 054303.
20 B. Meredig, A. Agrawal, S. Kirklin, J. E. Saal, J. W. Doak, A. Thompson, K. Zhang, A. Choudhary and C. Wolverton, *Phys. Rev. B,* 2014, **89**, 094104.
21 A. M. Deml, R. O'Hayre, C. Wolverton and V. Stevanović, *Phys. Rev. B* 2016, **93**, 085142.
22 X. Ma, Z. Li, L. E. K. Achenie and H. Xin, *J. Phys. Chem. Lett.,* 2015, **6**, 3528–3533.
23 Z. Li, S. Wang, W. S. Chin, L. E. Achenie and H. Xin, *J. Mater. Chem. A,* 2017, **5**, 24131–24138.
24 T. Toyao, K. Suzuki, S. Kikuchi, S. Takakusagi, K. Shimizu and I. Takigawa, *J. Phys. Chem. C,* 2018, **122**, 8315–8326.
25 Y. Nanba and M. Koyama, *J. Phys. Chem. C,* 2019, **123**, 28114–28122.
26 R. F. Zhang, X. F. Kong, H. T. Wang, S. H. Zhang, D. Legut, S. H. Sheng, S. Srinivasan, K. Rajan and T. C. Germann, *Sci. Rep.,* 2017, **7**, 9577.
27 R. Gasper, H. Shi and A. Ramasubramaniam, *J. Phys. Chem. C,* 2017, **121**, 5612–5619.
28 Y. Nanba and M. Koyama, *Bull. Chem. Soc. J.,* 2021, 94, 2484–2492.
29 G. Kresse and J. Furthmüller, *Phys. Rev. B,* 1996, **54**, 11169–11186.
30 G. Kresse and J. Furthmüller, *J. Comput. Mater. Sci.,* 1996, **6**, 15–50.
31 J. P. Perdew, K. Burke and M. Ernzerhof, *Phys. Rev. Lett.,* 1996, **77**, 3865–3868.
32 P. E. Blöchl, *Phys. Rev. B,* 1994, **50**, 17953–17979.
33 G. Kresse and D. Joubert, *Phys. Rev. B,* 1999, **59**, 1758–1775.
34 D. Wu, K. Kusada and H. Kitagawa, *Sci. Technol. Adv. Mat.,* 2016, **17**, 583–596.
35 J. M. Cowley, *Phys. Rev.,* 1950, **77**, 669–675.
36 S. Krüger, S. Vent, M. Staufer and N. Rösch, *Ber. Bunsenges. Phys. Chem.,* 1997, **11**, 1640–1643.
37 P. Nava, M. Sierka and R. Ahlrichs, *Phys. Chem. Chem. Phys.,* 2003, **5**, 3372–3381.
38 A. Roldán, F. Viñes, F. Illas, J. M. Ricart and K. M. Neyman, *Theor. Chem. Acc.,* 2008, **120**, 565–573.
39 Y. Nanba, T. Ishimoto and M. Koyama, *J. Phys. Chem. C,* 2017, **121**, 27445–27452.
40 T. Ishimoto, Y. Inadomi, H. Honda and M. Koyama, *J. Comput. Chem. Jpn.,* 2015, **14**, 52–53.
41 F. Wang and D. P. Landau, *Phys. Rev. Lett.,* 2001, **86**, 2050–2053.
42 D. P. Landau and F. Wang, *Comp. Phys. Commun.,* 2002, **147**, 674–677.
43 B. A. Berg and T. Neuhaus, *Phys. Rev. Lett.,* 1992, **68**, 9–12.
44 U. H. E. Hansmann and Y. Okamoto, *J. Comp. Chem.,* 1993, **14**, 1333–1338.
45 S.-H. Tsai, F. Wang and D. P. Landau, *Phys. Rev. E,* 2007, **75**, 061108.
46 D. P. Landau, F. Wang and S.-H. Tsai, *Comp. Phys. Commun.,* 2008, **179**, 8–12.
47 U. H. E. Hansmann, Y. Okamoto and F. Eisenmenger, *Chem. Phys. Lett.,* 1996, **259**, 321–330.
48 K. Kusada, H. Kobayashi, T. Yamamoto, S. Matsumura, N. Sumi, K. Sato, K. Nagaoka, Y. Kubota and H. Kitagawa, *J. Am. Chem. Soc.,* 2013, **135**, 5493–5496.
49 T. Ishimoto and M. Koyama, *arXiv* 2020, 2007.061737.
50 M. F. Michelon and A. Antonelli, *Phys. Rev. B,* 2010, **81**, 094204.
51 M. Mamatkulov, I. V. Yudanov, A. V. Bukhtiyarov, I. P. Prosvirin, V. I. Bukhtiyarov, K. M. Neyman, *J. Phys. Chem. C,* 2019, **123**, 8037–8046.

This journal is © The Royal Society of Chemistry 20xx

Phys. Chem. Chem. Phys., 2013, **00**, 1-3 | **9**

52 B. Farkaš, C. B. Perry, G. Jones, N. H. de Leeuw, *J. Phys. Chem. C,* 2020, **124**, 18321–18334.

Please do not adjust margins

52 B. Farkaš, C. B. Perry, G. Jones, N. H. de Leeuw, *J. Phys. Chem. C,* 2020, **124**, 18321–18334.